Finite element analysis of laser shock peening of 2050-T8 aluminum alloy

Neila Hfaiedh [a,*], Patrice Peyre [a], Hongbin Song [a], Ioana Popa [b], Vincent Ji [c], Vincent Vignal [b]

[a] PIMM, UMR 8006 CNRS- Arts et Métiers Paris-Tech, 75013 Paris, France
[b] ICB, UMR 5209 CNRS-University of Burgundy, 21078 Dijon, France
[c] ICMMO, University Paris-Sud, 91000 Orsay, France

ABSTRACT

Laser shock processing is a recently developed surface treatment designed to improve the mechanical properties and fatigue performance of materials, by inducing a deep compressive residual stress field. The purpose of this work is to investigate the residual stress distribution induced by laser shock processing in a 2050-T8 aeronautical aluminium alloy with both X-ray diffraction measurements and 3D finite element simulation. The method of X-ray diffraction is extensively used to characterize the crystallographic texture and the residual stress crystalline materials at different scales (macroscopic, mesoscopic and microscopic).

Shock loading and materials' dynamic response are experimentally analysed using Doppler velocimetry in order to use adequate data for the simulation. Then systematic experience versus simulation comparisons are addressed, considering first a single impact loading, and in a second step the laser shock processing treatment of an extended area, with a specific focus on impact overlap. Experimental and numerical results indicate a residual stress anisotropy, and a better surface stress homogeneity with an increase of impact overlap.

A correct agreement is globally shown between experimental and simulated residual stress values, even if simulations provide us with local stress values whereas X-ray diffraction determinations give averaged residual stresses.

1. Introduction

During the past 20 years, laser shock processing (LSP) has been proposed as a competitive alternative technology to classical surface treatments for improving fatigue, corrosion and wear resistance of metals. It has recently been developed as a practical process amenable to production engineering. This process (Fig. 1) aims at introducing a deep (mm range) residual compressive stress field on metallic targets.

More precisely, LSP uses high energy laser pulses (in the GW/cm² range) to impact the surface of a metal coated with a protective film (organic paint, tape or thin metallic film), and covered with a transparent layer (usually water). As the laser beam passes through the transparent layer and hits the surface of the material, a thin layer of the ablative layer is vaporized (nearly 1 μm/shot). The vapor continues to absorb the remaining laser energy and is heated and ionized into a high pressure plasma. Due to the confining effect

of the transparent layer, the plasma pressure is amplified (up to several GPa), and the resulting pressure discontinuity propagates into the material as a shock wave [1,2]. This plasma confined regime, allows obtaining maximum impact pressures of up to 5–6 GPa in the 8–10 GW/cm² intensity regime for 10–20 ns pulse duration, as experimentally shown in [3].

In turn, the shock wave can cause plastic deformation and compressive stresses, provided the plasma pressure is of sufficient magnitude to exceed the Hugoniot Elastic Limit (HEL) of the metal. Consequently, the specimen will undergo extremely high strain-rate (greater than $10^6 \, s^{-1}$) during a short period of time ($\cong$10–20 ns in our case) and be dynamically yielded.

Recent developments of industrial systems have been proposed by some companies [4–6] using either low output energy (around 1 J/pulse) or higher energies (20–40 J/pulse) lasers [7,8]. They have shown the feasibility of using LSP in an industrial environment, with a large range of configurations (between 5 mm and 10 μm diameters of impacts), materials and applications. The benefits of the treatments versus other impact treatments (shot-peening, ultrasonic peening, deep rolling) are rather well known: a rather
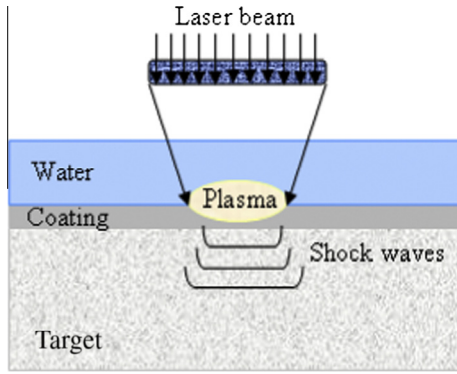
Fig. 1. Laser peening process.

good preservation of surface roughness, large affected depths (superior to 1 mm), and nearly the same amplitude of compressive stresses at the surface of metallic materials.

To predict the residual stress field and optimize laser shock parameters, several experimental and analytical formulations have been reported in the literature, starting by the early analytical work by Ballard [9]. The Finite Element Method (FEM) was first introduced by Braisted and Brockman [10] to predict the residual stresses induced by LSP on carbon steels using Abaqus software, and a combined explicit + implicit approach in 1999. From then on, several researchers have used Abaqus to analyse laser shock waves propagation into different metal materials, and the resulting residual deformations and stresses [11–14]. Some of these simulations have shown a close match with experimentally measured residual stresses. A recent work has also developed a three-dimensional FEM model to simulate a metal subjected to a square laser spot [15] using the ANSYS code. Last, we can mention the recent work by Hirano et al. [16] who has demonstrated for the first time analytically, that residual stresses induced by LSP could be anisotropic.

Most of these numerical works have usually considered average in-depth stresses induced by LSP, without really addressing surface stress gradients, and their dependence with LSP conditions such as overlapping rate, or spot diameters. Moreover, the validation of pressure loading conditions $P = f(x,y,t)$, or material's behavior under purely uniaxial shock conditions was not systematically addressed.

In the light of the above discussion, a 3D numerical model was developed with different objectives: (1) identifying pressure loading and shock yield stress using both Doppler velocimetry, and single impact analysis, (2) making systematic comparisons between measured and calculated residual stresses for different LSP conditions, (3) investigating numerically surface stress gradients, and their dependence with overlapping rate, (4) for the same overlapping rate, spot diameter, and impact pressure, investigating the influence of different LSP paths.

More precisely, the time and spatial distribution of the loading pressure $P = f(x,y,t)$ could be identified by checking surface deformations induced by a single laser impact, using both 2D profilometry and numerical simulation, using an analytical formulation for the pressure. In a second step, the LSP treatment of an extended area is considered, using up to 25 impact loading, and addressing different LSP parameters such as laser spot sizes, pressure amplitude, or overlapping rate.

2. The base 2050-T8 Al alloy

The material under investigation in this paper is a 2050-T8 aluminium alloy (AA) which is mainly composed of 3.5 Cu, 0.9 Li, 0.3 Mg, 0.4 Mn, 0.05 Fe and Al in weight %. This material, recently developed for structural aerospace application, has a high elastic limit (0.51 GPa), due to Al$_2$Cu nanometric precipitation strengthening. In addition, grain sizes ranging between 20 μm and 500 μm were identified by EBSD analysis, with a texture orientated along the rolling direction [17]. The resulting mechanical properties are illustrated in Table 1.

3. Experimental setup and procedures

3.1. LSP conditions

The 2050-T8 alloy was laser-peened with a Nd:YAG pulsed laser, producing 10 ns duration pulses with up to 1.5 J per pulse at 0.53 μm. The 0.53 μm wavelength allowed us to use large water thickness without generating extended laser light absorption. Using our classical LSP configuration, the target was completely immersed in water (5–10 cm thick), and a high pressure water nozzle was used to remove ablation dusts. Classically, 1–2 mm diameter impacts were used, with intensities in the 3–8 GW/cm^2 range corresponding to estimated pressures in-between 2 GPa and 5 GPa using empirical equation $P\ (\text{GPa}) = 1.65 \cdot \sqrt{I(\text{GW/cm}^2)}$ [18] and the LSP treatment of extended areas could be achieved by the overlap of successive spots until the desired region was completely covered. Prior to LSP treatment, 8 mm-thick aluminium samples were protected from thermal rise by a 80 μm-thick aluminium adhesive, and a 10 μm organic paint, to ensure a pure mechanical loading on targets.

In this work, we imposed a fixed number of identical and overlapped pressure pulse impacting a target material successively as shown in Fig. 2. Two main directions were considered: the σ_{xx} ($\cong\sigma_{11}$) stresses parallel to the LSP direction and the σ_{yy} ($\cong\sigma_{22}$) stresses perpendicular to the main LSP direction. In addition, the overlapping rate $R\%$ was defined by ($=\Delta d/d$ with d = impact diameter and Δd = distance between two impacts). Different overlapping rates will tend to modify surface topography as shown in Fig. 3a (33% overlap) and Fig. 3b (50% overlap).

3.2. VISAR determination of impact pressures and elastic precursors

The measurement of impact pressure and shock yield strengths were both carried out by VISAR (Velocity Interferometer System for Any Reflector) Doppler velocimetry. This technique already used successfully in the past 15 years [18,19], allowed us, by a simple measurement of back free surface velocities U_F (m/s) behind thin foils to analyse shock wave propagation, and deduce the $P = f(t)$ profiles on 1.5 mm diameter impacts, using Hugoniot conservation equations ($P = 1/2\rho \cdot D \cdot U_F$, with D = sound velocity (m/s), and ρ = density (kg/m^3))[1].

A back free velocity profile obtained behind a 430 μm-thick 2050-T8 foil is shown in Fig. 5. The maximum velocity can be

---

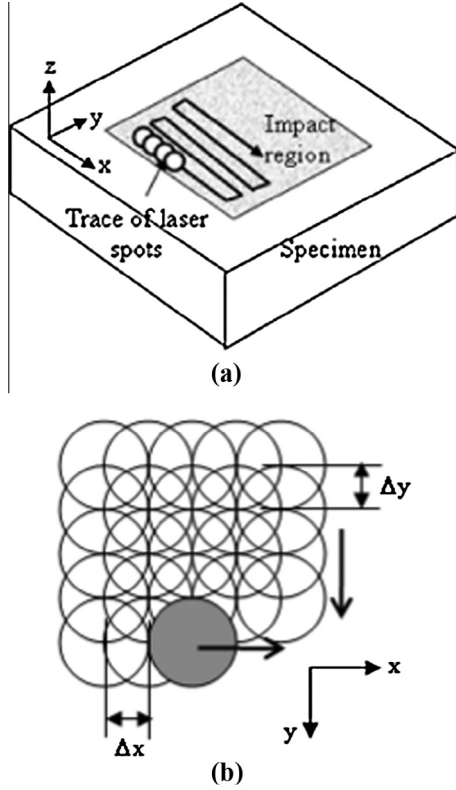[1] For more details about VISAR determinations, please refer to [15–17]

(a)

(b)

Fig. 2. (a) The overlapping laser shock processing, (b) LSP treatment with 50% overlapping rate.
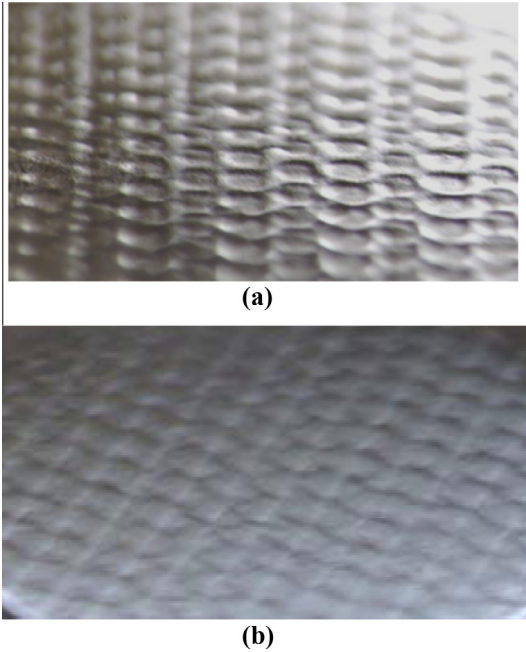

(a)

(b)

Fig. 3. Surface topography after – (a) a 33% overlap LSP, (b) a 50% overlap LSP (1.5 mm spot diameters, 5 GW/cm² power density).

directly related to the pressure amplitude 500 μm below the surface, whereas the inflexion evidenced in the shock rise time is known as the elastic precursor, and corresponds to the elastic–plastic transition under uniaxial shock loading. On Fig. 5, a 170 m/s velocity level is evidenced at the elastic–plastic transition,
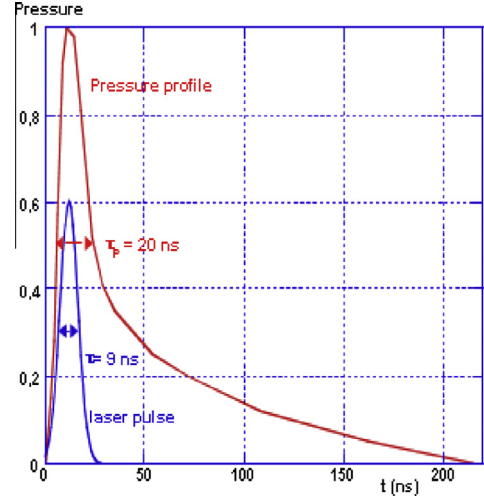

Fig. 4. Normalized pressure pulse induced by a 8–10 ns laser pulse (resulting in a 20 ns width at half maximum) used in ABAQUS.
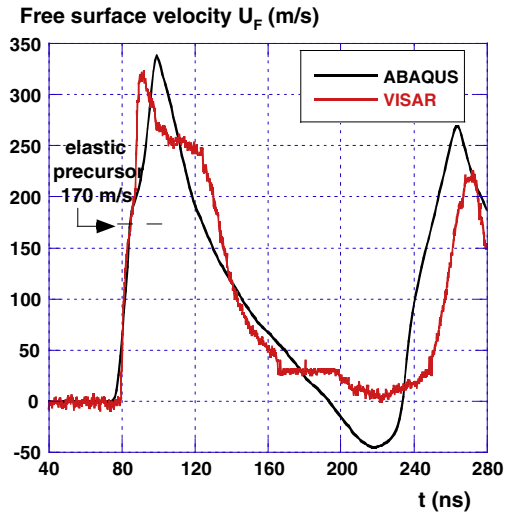

Fig. 5. Determination of the elastic precursor (inflexion at 170 m/s) and shock yield stress using back free velocity U_F measurements on a 430 μm-thick 2050-T8 foil (I = 5.5 GW/cm², surface pressure = 3.8 GPa)-comparison with Abaqus simulation.

which corresponds to a 1.38 GPa yield stress under planar laser-shock loading (or Hugoniot limit) P_H (see Eq. (1)).

$$P_H = \frac{1}{2}\rho \cdot C_{el} \cdot U_F \tag{1}$$

With C_{el} = elastic wave velocity = 6000 m/s, ρ = 2750 kg/m³.

The determination of P_H allows us to determine the strain rate sensitivity as an input data for constitutive Johnson–Cook's Eq. (3) using the following formula:

$$P_H = \frac{1-\upsilon}{1-2\upsilon}\sigma_y^{dyn} \tag{2}$$

With υ = anisotropy Poisson's coefficient (0.33 on 2050-T8), σ_y^{dyn} = dynamic Yield stress at 10^6 s⁻¹.

In turn, using P_H = 1.38 GPa we obtain a dynamic yield stress value σ_y^{dyn} equal to 0.7 GPa, and a strain rate sensitivity coefficient C = 0.02 (for σ_Y = 0.51 GPa). The C value was estimated by checking the elastic precursor (=P_H) value with a VISAR interferometer system [15].

Therefore, using VISAR measurements, $P = f(t)$ profiles (Fig. 4), and shock yield stress (Fig. 5) could be determined and used as input data in the numerical simulation.

3.3. Residual stress determination using the XRD technique

The residual stresses were measured using the well known X-ray diffraction, using two different conditions, both corresponding to a 10–11 μm penetration depth of X-rays. The X-rays patterns were first recorded using a SET-X device with a 20 kV voltage, a 5 mA intensity, and a 1.5 mm diameter X-ray spot. The classical $\sin^2\psi$ method was used to determine residual stresses, selecting {3 1 1} as a diffracting plane because of a low anisotropy effect of the material. The corresponding diffraction conditions are summarized in Table 2.

Recent developments based on micro X-ray diffraction (μXRD) have allowed us to extend X-ray examination to a microscopic level, using a 100 μm diameter probe X-ray beam. μXRD uses specific optics to focus the excitation beam to a small spot on the sample surface so that very local areas can be analysed on the sample. The measurements have been realized in ICB laboratory, using a Brucker diffractometer, with a Cu source, theta–theta geometry, Gobel mirror parallel optics with 50–500 μm collimator, and a 2D detector (Table 3).

4. Initial conditions and work-hardening levels

The surface analysis was carried out by XRD on the surface of the sample before and after LSP treatment. Before LSP treatment (Fig. 6a), residual stresses attributed to mechanical polishing have a low amplitude (−40 MPa), are homogeneous and isotropic ($\sigma_{11} \approx \sigma_{22}$).

In addition, the study of the integral width of X-ray peaks provides useful information about work-hardening. In Fig. 6b, a small variation of peak width is evidenced after LSP (+5% to 20%), which confirms the limited work-hardening induced by LSP on 2050-T8 alloy (Fig. 7). Vickers Hardness tests were also carried out at the surface of impacted materials, with a 25 g load resulting in nearly 20 μm indent sizes, and 5 μm indented depths. Results indicate rather similar hardness variations (+35%) than X-ray peaks integral widths, from 1.2 GPa average value for the as-polished condition, up to 1.6 GPa mean value after LSP treatment. The scattering observed on Vickers measurements may be attributed to grain orientations versus shock loading main direction, that promote or not dislocation formation. Such limited work-hardening levels are consistent with most of previous works on aluminum alloys after LSP treatments [14,20].

5. 3D simulation of the LSP process

5.1. Description of the numerical model

In most of recent FEM analysis procedures of LSP [11,13,15], two distinct steps were considered to obtain an absolutely stable

Table 2
Diffraction condition using Set-X diffractometer.

Cr anode	$\lambda k\alpha = 0.229$ nm
Filter	V
Collimator	1.5 mm
Plans {$h k l$}	{3 1 1}
Number of ψ angles	15
Oscillations of ψ	+/−5
Acquisition time (s)	100 s

Table 3
Diffraction condition using Brucker diffractometer.

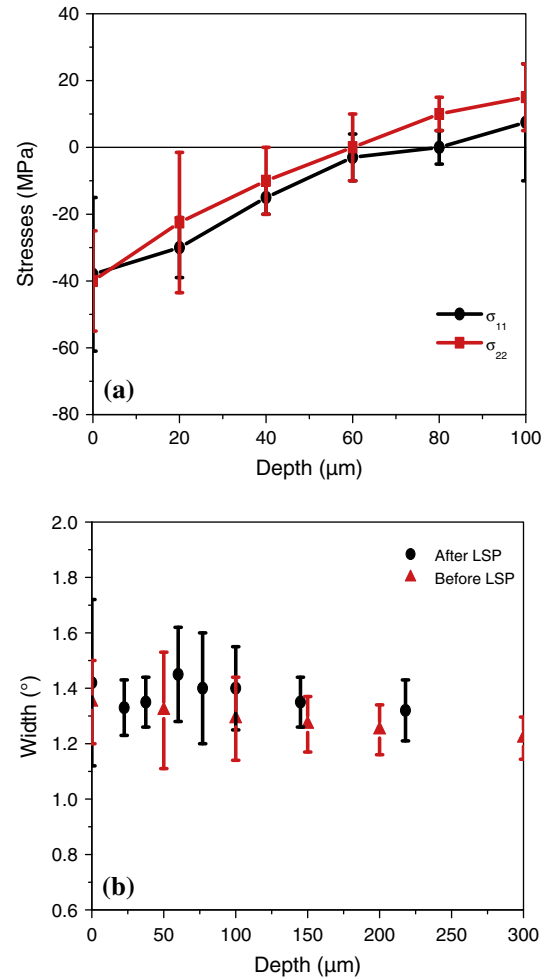|	
Cu anode	$\lambda k\alpha = 1.709$ nm
Filter	V
Collimator	0.5 μm
Plans {$h k l$}	{3 1 1}
Number of ψ angles	22
Oscillations of ψ	+/−5
Acquisition time (s)	100 s

Fig. 6. (a) Initial residual stresses of AA2050-T8, σ_{11} (rolling direction) and σ_{22} (transverse direction), (b) influence of LSP on the integral widths of X-ray peaks (5 GW/cm² – 50% overlap).

residual stress field: (1) a dynamic explicit analysis to investigate shock wave propagation and (2) a static analysis using an implicit algorithm to calculate residual stress fields. In our case, a single explicit dynamic calculation was selected to estimate directly a quasi-residual stress field, for a large number of impact loadings. A 3D finite element model was developed on ABAQUS™ 6.9 Explicit software to simulate the LSP process, including for each impact shock propagation and relaxation in a single step.

A schematic of the 3D model is shown in Fig. 8. Infinite elements have been adopted as non-reflecting boundaries to avoid shock wave reflections on free surfaces. Up to 2759918 continuum solid hexahedral linear elements were used to mesh a 25 mm × 25 mm × 5 mm body, resulting, with the use of a BIAS geometrical function allowing a mesh refinement, in 100 μm × 100 μm × 10 μm element sizes near the impacted surface.
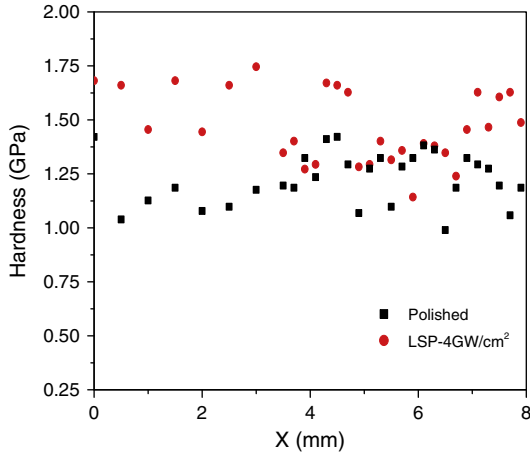
Fig. 7. Vickers hardness distribution after LSP treatment (5 GW/cm² – 50% overlap).
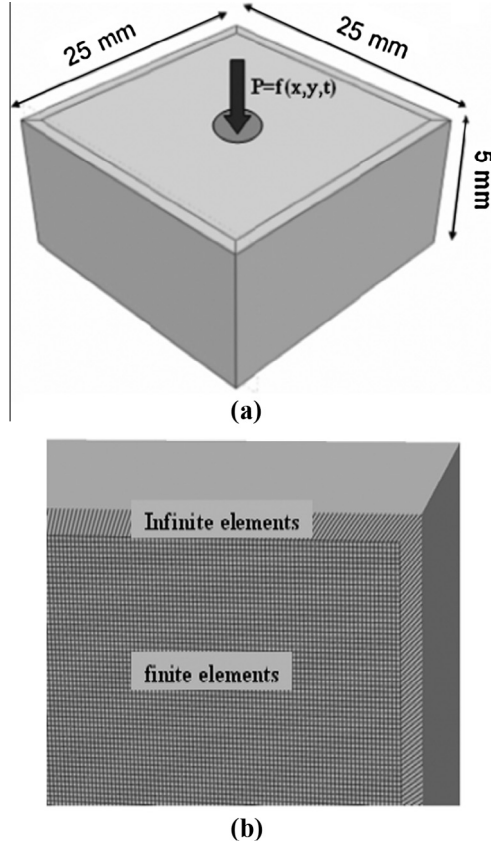

Fig. 8. (a) The 3D model, (b) detailed view of finite and infinite elements.

The use of very thin elements, allowed us to consider correctly the stress wave propagation (at C_0 speed) near the surface for a 20 ns duration pressure pulse.

Before using the numerical description of laser shocks, a convergence test was carried out [11] in order to define optimal integration times for the calculation (by default, Abaqus Explicit provided us with an integration time of $t_0 = 8.6$ ns for our meshing conditions). At least a factor 4 reduction of this time ($t_0 = 2$ ns) was shown to provide constant stresses and deformations.

In addition, when simulating several impacts applied at different locations and times, a minimum time interval between

successive impacts had to be selected to ensure a quasi-residual stress field. Above 10^{-5} s time interval, the kinetic energy of the 3D body was shown to turn to a near-zero value (Fig. 9), thus allowing us to simulate multiple stabilized impacts. It has to be mentioned that this time period for the global calculation of one impact (shock + relaxation) appears to be much longer than the pressure loading duration itself (200 ns in Fig. 3).

Following this, the in-depth stress wave attenuation could be checked accurately (Fig. 10), for different propagation times t_i and positions – z (with $z = D·t_i$ with D = sound velocity).

5.2. Constitutive material's behaviour

Due to the high strain rate involved during LSP events (near 10^6 s^{-1}), the Johnson–Cook stain sensitive plasticity model is classically used for problems where strain rates vary over a large range. If ε_p is the equivalent plastic strain, the Von Mises flow stress, according to the Johnson–Cook model, is given by:

$$\sigma = (\sigma_y + K\varepsilon_p^n)\left[1 + CLn\left(\frac{\dot{\varepsilon}}{\dot{\varepsilon}_0}\right)\right]\left[1 - \left(\frac{T - T_0}{T_{melt} - T_0}\right)^m\right] \quad (3)$$

where σ_y, K, C, n, and m are material constants (σ_y = yield stress, K and n = work-hardening modulus and coefficient, C strain rate sensitivity, T_{melt} = fusion temperature, etc.).

For our experimental conditions, preliminary investigations using fully coupled thermo-mechanical-elements DC3D8T confirmed that the thermal contribution of Eq. (3) could be neglected: on a single 4 GPa–20 ns impact, the local thermal rise due to shock wave propagation and plastic deformation was less than 40 K, and did not modify significantly the residual stress field, even with a 100% inelastic heat fraction. Consequently, the thermal part of Johnson–Cook's equation was omitted in our simulation. Corresponding Johnson–Cook's coefficients for 2050-T8 are presented in Table 4. The $C = 0.02$ value was experimentally determined by VISAR measurements of dynamic Yield stress (see Section 3.2).

5.3. Simulation of a single laser impact

The simulation of a unique laser impact and its validation using experimental data has nearly never been addressed in the literature. Our objective was twice: (1) validating the pressure spatial
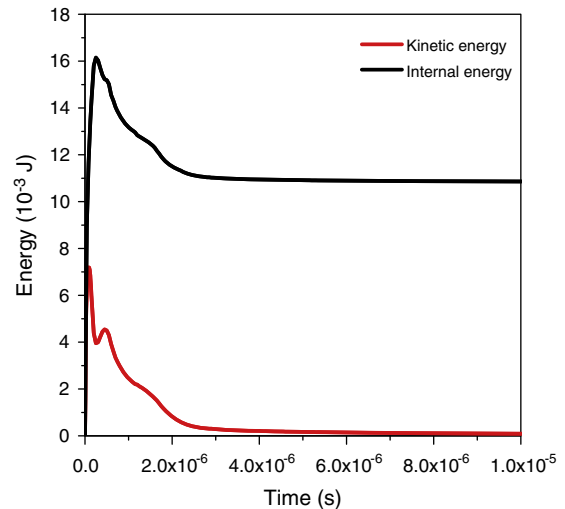

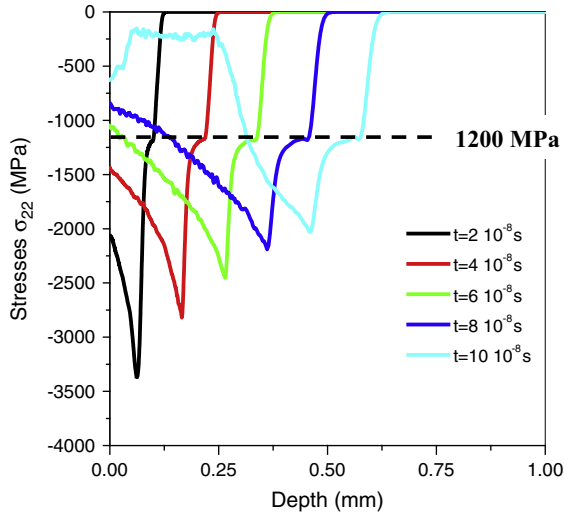**Fig. 9.** Kinetic and internal energy from 10^{-5} s.

Fig. 10. Stress wave propagation for a $P = 3$ GPa incident pressure corresponding to $I = 3.5$ GW/cm^2.

Table 4
Johnson–Cook's coefficients for 2050-T8.

σ_y (MPa)	510
K (MPa)	200
n	0.45
C	0.02
$\dot{\varepsilon}_0$	0.01

distribution $P = f(x,y)$, (2) validating the model by checking the residual stress field, using a μ X-ray diffraction technique.

5.3.1. Identification of the spatial pressure distribution $P = f(x,y)$

A fortran subroutine was used (*VDLOAD type) to generate non-uniform spatial and temporal loadings $P = f(x,y,t)$ and locate precisely impact position. The $P = f(x,y)$ distribution was adjusted to fit exactly experimental surface deformations $u_{33} = f(x)$ for a given laser intensity I (W/cm^2). Considering a single 1.5 mm impact ($r_0 = 0.75$ mm), and a maximum available impact pressure

$P = 5$ GPa, the best agreement with experimental results (Fig. 11) was found for a near-spherical spatial distribution of pressure (Eq. (4)). The corresponding maximum deformation u_{33} induced by a single impact is shown to be approximately -10 μm. This allowed us validating the $P = f(x,y,t)$ loading for the calculation of a large number of laser impacts.

$$P(x, y, t) = P_0(t)\sqrt{1 - \frac{1}{2}\left(\frac{x^2 + y^2}{r^2}\right)} \qquad (4)$$

5.3.2. Determination of residual stresses on a single 1.5 mm impact

In this section, we considered the pressure dependence of residual stresses for a single impact, together with an experimental validation using the micro X-ray diffraction technique [21], and the classical $2\theta = f(\sin^2\psi)$ method. A 50 μm X-ray collimator was used at ICB-Dijon for analyzing stress distributions, corresponding, after beam divergence to a 100 μm XRD spot on the metal.

Simulations indicate an interesting and important result: the stress drop at the centre of circular impacts seems to be promoted by the use of high pressures: a 3 GPa pressure provides less homogeneous stress field than a 2 GPa pressure (as we can see in Fig. 12). Indeed, for the case of 3 GPa applied pressure, a pronounced stress singularity appears.

The comparison between experimental and simulated residual stress values was shown to indicate a 100 MPa overestimation of residual stress amplitude (-300 MPa versus -200 MPa) using a 2 GPa impact pressure. Two factors may explain why the experimental to numerical comparison is not that satisfactory on one impact: (1) the μXRD patterns are mostly obtained inside grains on very small diffracting crystallites that may not be representative for the global aluminium diffraction constants, (2) the experimental residual stress field is overwhelmed by the central stress drop, which is more pronounced and extended than numerically predicted.

We analysed the residual stresses in the depth (see Fig. 13), we noted that the stress field heterogeneity is focused to the surface of the material in a depth about 250 μm for $P = 2$ GPa and 675 μm for $P = 3$ GPa. The depth of compressive zone increase with the applied pressure P. This is due to the plastic flow increasing with respect to the applied pressure.
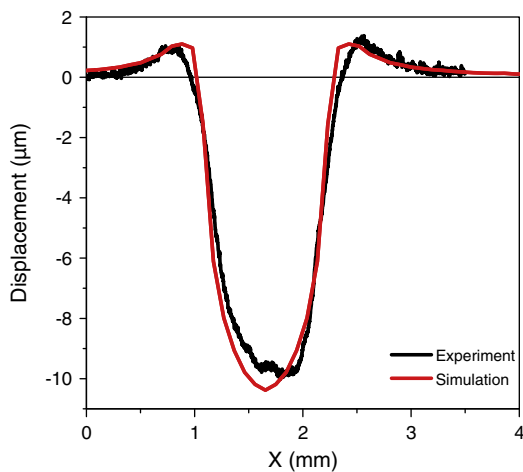

Fig. 11. Comparison between experimental and simulated single laser impact: 1.5 mm – 8 GW/cm^2 impact (5 GPa) simulation with a spherical $P = f(x,y)$ distribution.
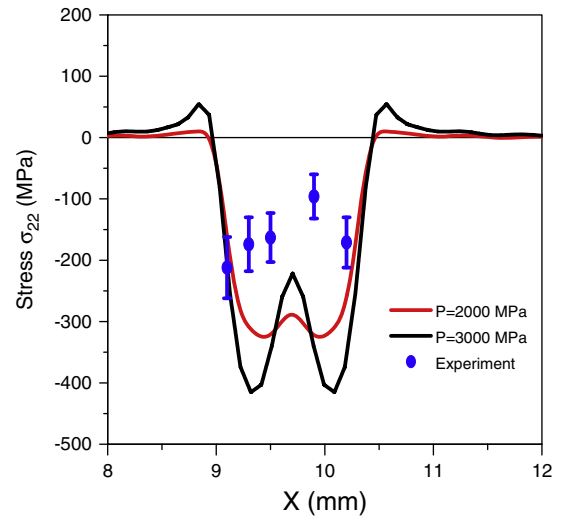

Fig. 12. FEM simulation of residual stresses induced by a 1.5 mm impact for 2 and 3 GPa. Comparison with μXRD measurements carried out on a single 3.5 GW/cm^2 impact.
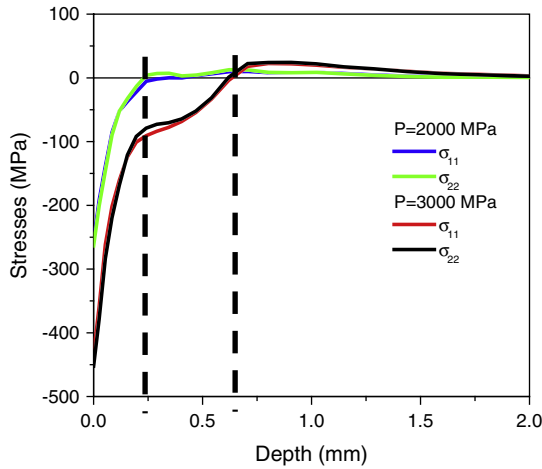
Fig. 13. FEM simulation of in depth residual stresses by 1.5 mm impact at 2 and 3 GPa (simulations considered at $r_0/2$).
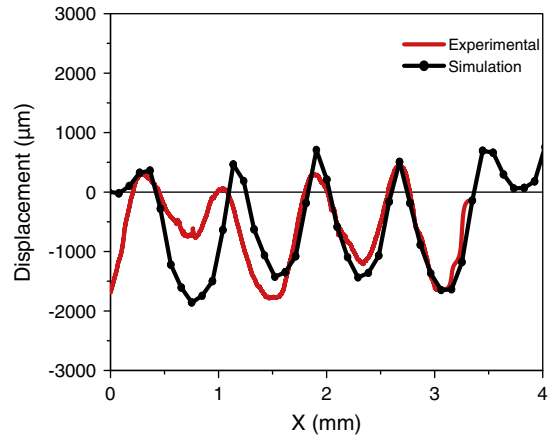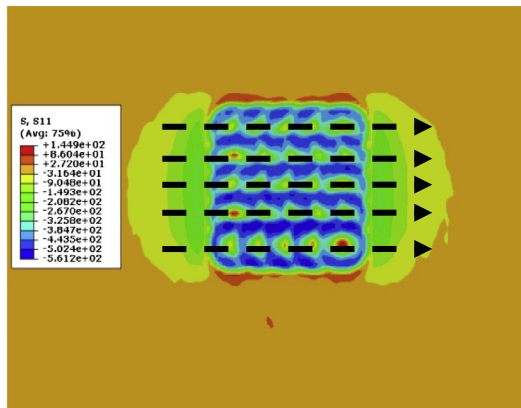

(a)

(b)

Fig. 14. FEM simulation of residual stresses by 1.5 mm impacts at 3 GPa (3.5 GW/cm²), overlapping 50% (a) σ_{11}, (b) σ_{22}.
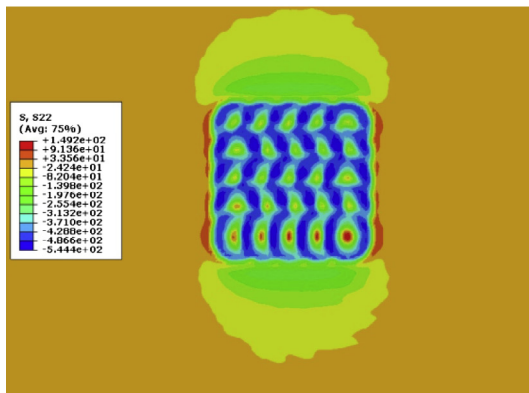

Fig. 15. Experimental versus simulated surface deformation u_{33} induced by 25 laser impacts (1.5 mm – 3.5 GW/cm² – 50% overlap) – simulation with a spherical $P = f(x,y)$ distribution and $P = 3$ GPa maximum pressure.
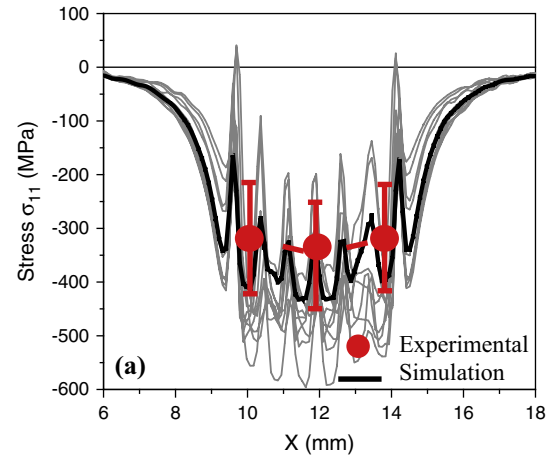

(a)

(b)

Fig. 16. XRD experiments versus simulations, 25 impacts, $d = 1.5$ mm at $P = 3$ GPa, overlapping 50% (a) σ_{11}, (b) σ_{22}.
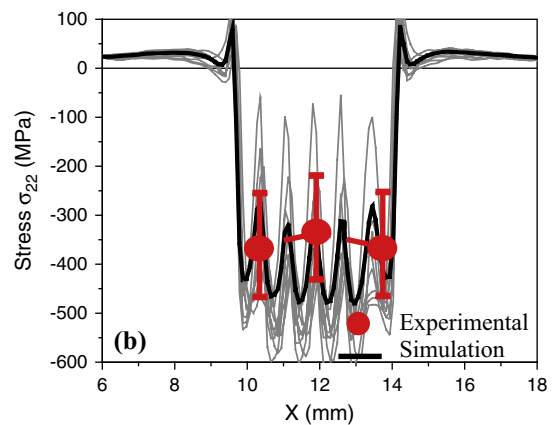
5.4. Simulation of 25 overlapped impacts

Results of the simulations of 25 impacts on 2050-T8 are presented in Figs. 14–16, for a classical LSP path (50% overlap and a continuous line by line y increment: Fig. 3), which corresponds to the surface finish presented in Fig. 3b.

These simulations indicate a strongly heterogeneous and periodic surface stress field (Fig. 14a and b), attributed both to impact overlaps, and to the stress drops at the centre of circular impacts. Approximately 100 to 200 µm thick layers are affected by this

stress heterogeneity. Below 200 µm in-depth, the stress field becomes much more homogeneous.

The comparison of simulation with experience was made using: (1) 2D profilometry, (2) conventional surface X-ray diffraction (1.5 mm XRD spot), (3) in-depth XRD diffraction using matter removal.

The experimental and numerical analysis of residual stresses on x and y axis (with x = main LSP axis: cf Fig. 3a and b), indicates an anisotropic stress generation, already investigated analytically by Zhang et al. [13].

The σ_{22} stresses (Figs. 14b and 16b) are always higher than σ_{11} stresses (Figs. 14a and 16a), independently of the initial rolling direction of the base material. This result has never been pointed out experimentally by many authors except by [22] on aluminium alloys. This result is globally confirmed by simulations, where local σ_{22} values are more compressive than σ_{11} values.

The appearances of tensile stress, in red local area as we can see in Fig. 14, are harmful in fatigue. Fortunately, this critical problem is reduced by the overlap and remains in the boarders of the LSP treated area. So to avoid this harmful problem we just manage the LSP treated area in such manner to move away these critical area from the most mechanically stressed zones.

The comparison between simulated and experimental surface deformations is satisfactory (Fig. 15). The periodic deformation, and its maximum amplitude u_{33}^{max} is shown to be nearly the same (1.7 mm), even if finer meshes would have possibly improved numerical data, and more specifically the shape of peak curvatures, which are shown to be sharper on simulations than on experiments.

A comparison of numerical simulations with XRD surface determinations, carried out with 1.5 mm XRD spot diameters first requires an averaging of σ_{11} and σ_{22} simulated profiles as shown in Fig. 14a (black arrows), to allow comparison at the same scale. Similarly, in-depth simulated stresses also correspond to averaged data, considered using 12 in-depth lines located inside a 1.5 mm diameter circle.

The corresponding surface averaged values are shown in Fig. 16a and b (black line) and compared with XRD determinations. For a 4–5 GW/cm^2 – 50% overlap condition, the comparison of σ_{11} values shows that experimental values ($\cong$−350 MPa) are found in-between higher and lower simulated residual stresses values, but are approximately 100 MPa lower in amplitude than average simulated values ($\cong$−350 MPa). If we now consider the non-averaged simulated profiles (in grey lines on Fig. 16a and b), the oscillating aspect of residual stress profile at 50% overlap provokes large local stress maximum gradients ($\sigma_{11}^{max} - \sigma_{11}^{min}/\Delta x$), estimated to 0.5 MPa/μm.

The difference between averaged simulated stresses and measured data is nearly the same for σ_{22} values, but with even more pronounced simulated stress gradients near 1.4 MPa/μm. Such sharp residual stress gradients, that would necessitate to be confirmed by micro-X-ray diffraction tests (but with extremely long acquisition time), would play an active role on surface reactivity in electrochemical environment, by the formation of local galvanic coupling phenomena [23].

In-depth comparisons (Fig. 17), using averaged profiles, indicate a rather good correlation for impact pressures ranging between 2 GPa (3 GW/cm^2) and 3 GPa (5 GW/cm^2) as shown in Fig. 16a and b. They also indicate that anisotropy effects ($\sigma_{22}-\sigma_{11}$) are mostly superficial and seem to be restricted to the first 0.1–0.2 mm in depth.

5.5. Influence of percentage overlap

If we now check the influence of different percentage overlaps (A%), ranging between 33% and 66%, on the surface stress field, we can make the following remarks:

(1) The average surface stress tends to increase with A%: −340 MPa to −410 MPa for σ_{11}, and −350 to −420 MPa for σ_{22}.
(2) Increasing the percentage overlap rate A% (from 33% overlap to 66% overlap) tends to reduce surface stress gradients (Fig. 18), and therefore favours surface stress homogeneity by smoothing the residual surface stress field. This is shown
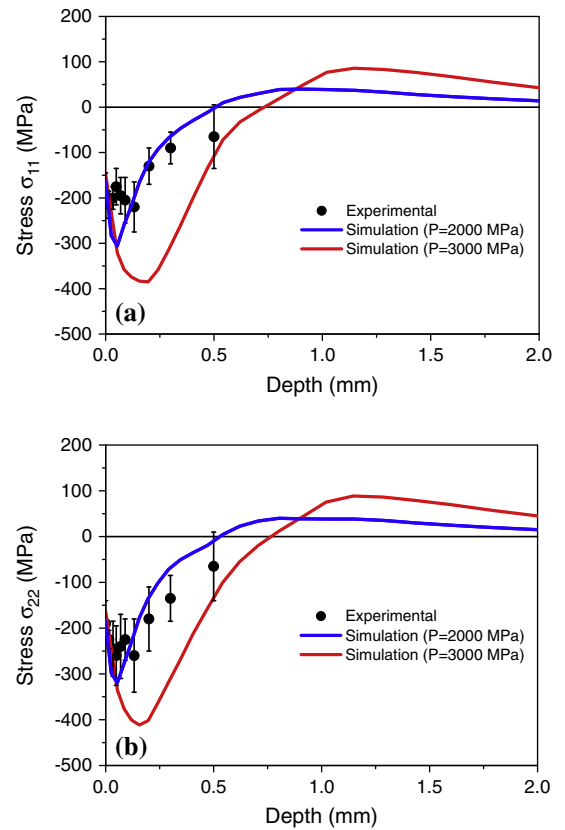

Fig. 17. Influence of impact pressure on in-depth residual stress profile (d = 1.5 mm, 50% overlap) (a) σ_{11}, (b) σ_{22} (simulation results are averaged values using 12 in-depth profiles considered inside a 1.5 mm diameter circular area similar to XRD spot).

on average values in Fig. 18, but is even more pronounced considering maximum stress gradients from local simulated stresses (Table 5).

The geometrical effect of stress concentration, which must be calculated with the depth of the indentations and the curvature radius. With LSP, this effect s is significantly lower than the curvature radius induced by shot peening.

5.6. Influence of different LSP strategies

Compared with a classical shot-peening treatment where beads randomly impact surfaces, laser-shock peening allows programming not only the precise position of each impact, but also the global-and possibly complex-time sequence of a large number of impact loadings. In turn, LSP can be considered as a deterministic mechanical surface treatment, where impact chronology relative to each other is expected to play a significant role on local stress amplitudes and gradients.

To confirm this assumption, another LSP path (or strategy) was tested (Fig. 19) where LSP treatment is not geometrically continuous, and where LSP lines are progressively fulfilling a free space, from two external lines, but with a similar 50% percentage overlap. The resulting chronology of impacts is different.

Simulation results indicate clearly that such a change of LSP path does not modify the global shape of residual stress field in itself, but affects significantly local stress amplitudes and gradients. On specific areas, the 2nd strategy generates lower stress amplitudes (Fig. 20) than the classical configuration. Consequently, these preliminary results confirm that impact chronology, and
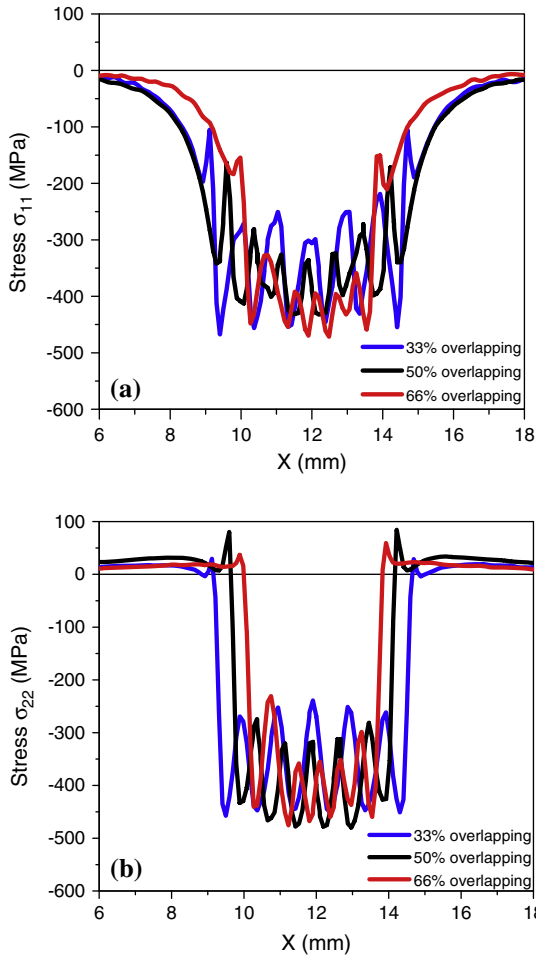
Fig. 18. Influence of percentage overlap (33%, 50% and 66%) on the surface stress distribution: (a) σ_{11}, (b) σ_{22}.

Table 5
Influence of percentage overlaps $A\%$ on the maximum local surface stress gradients.

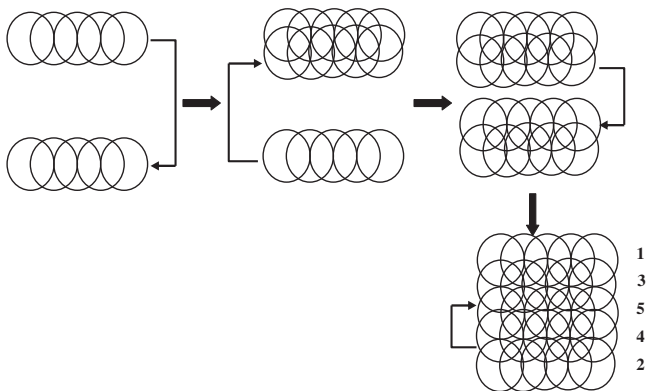|	$(\sigma_{11}^{max} - \sigma_{11}^{min})/\Delta x$
$A = 33\%$	0.7 MPa/μm
$A = 50\%$	0.5 MPa/μm
$A = 66\%$	0.25 MPa/μm

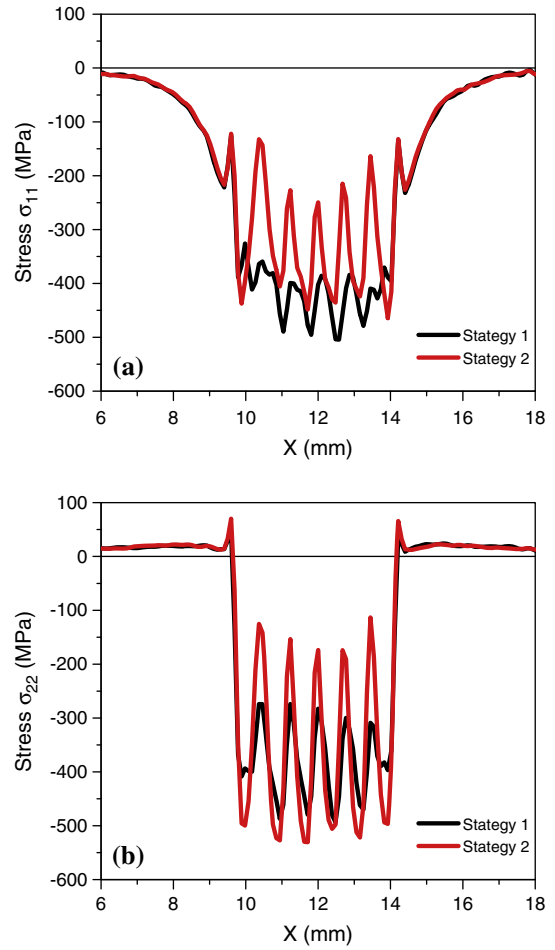**Fig. 19.** Surface treatment with a non-continuous LSP path.

Fig. 20. Effect of LSP strategies on FEM simulation of average residual stresses (25 impacts, d = 1.5 mm, P = 3 GPa, 50% overlap), (a) σ_{11}, (b) σ_{22}.

more widely, the LSP strategy can be considered as a non-negligible contributor to RS generation.

6. Discussion

A 3D model has been proposed for simulating residual stresses induced by LSP, with a particular focus on several aspects:

The use of experimental validations for impact loading, shock yield stress, and the XRD measurement of residual stresses induced either by one single impact, or by a large number of impact overlaps;

The FEM analysis of surface stress distribution, and surface stress gradients, which has never been extensively considered in the past.

The critical point to address concerning this model came from the XRD validation of numerical simulations which provided us with integrated values whereas simulations calculated local stresses. To overcome this issue, we considered averaged simulation values to be compared with XRD data, and this allowed us to globally validate the complex and heterogeneous residual stress field induced by LSP.

An attractive solution would have certainly been to make residual stress mappings using the micro-diffraction technique (0.1 mm spot), that we used for analyzing one single impact. However, this technique is extremely time consuming and a global mapping of a large number of impacts would have been impossible.

To obtain better experimental data on residual stress local gradients, future prospects should certainly use materials with small grains, allowing using smaller XRD collimators.

A last point to be mentioned is the precise knowledge of LSP conditions: the estimation of impact pressures was made using an empirical model where pressure can be directly calculated from the laser intensity value I (GW/cm^2). This necessitates a precise determination of impact diameter which is not that obvious when impacts are small (1–2 mm). Indeed, laser spot diameter is somewhat different (smaller) than impact diameter, due to lateral expansion of the plasma. In turn, a 1.5 mm diameter impact can be due to a 1.2 mm laser spot. This could explain why laser intensities I (GW/cm^2) presented in this paper include a significant error bar, because of an approximately 10–20% incertitude on impact diameter.

The anisotropy effect, predicted analytically [16], and evidenced on 2050-T8 alloy (and previously on another Al alloy: 6056-T4 [24]), seems to be rather specific to aluminium alloys, but should be investigated more widely to understand the singularity of such materials versus LSP treatment.

Last, numerical results indicate severe surface stress gradients due to impact overlaps which could play a significant role on surface reactivity by generating galvanic coupling between low and high amplitude local stress areas. The validation of such a heterogeneous surface stress field should require further experiments on materials with much smaller grains allowing determining more local stresses with smaller XRD collimators (0.5 mm).

The use of microdiffraction, possible on a single impact (each measurement takes approximately 2 h X-ray counting time on each direction), cannot be envisaged for characterizing a large peened surface.

7. Conclusions

A 3D numerical model for laser shock processing has been proposed, and validated experimentally on 2050-T8 al alloy. A tendency to residual stress anisotropy, and large surface stress gradients were shown to be the main factors describing LSP-induced residual stress fields. Future prospects should consider materials with small grains to improve experimental versus calculation comparisons.

Acknowledgement

References

[1] Fabbro R, Fournier J, Ballard P, Devaux D, Virmont. J physical study of laser produced plasma in confined geometry. J Appl Phys 1990;68:775–84.
[2] Clauer AH, Holbook JH, Fairand BP. Shock waves and high-strain-rate phenomena in metals. Concepts and Appl., (Plenum New York) 1981;675–702.
[3] Peyre P, Berthe L, Fabbro R, Sollier A. Experimental determination by PVDF and EMV techniques of shock waves induced by 0.6 to 3 ns laser pulses in confined regime with water. J Phys D: Appl Phys 2000;33:498–503.
[4] Mannava S, McDaniel AE, Cowie WD. General electric company (Cincinnati, OH). US Patent; 1996;5,492,447.
[5] Mannava S, McDaniel AE, Cowie WD. General electric company (Cincinnati, OH). US Patent, 1997;5,591,009.
[6] Casarcia DA, Cowie WD, Mannava S. General electric company (Cincinnati OH). US Patent, 1996;5,584,586.
[7] Sano Y, Kimura M, Sato K, Obata M, Sudo A. Development and application of laser peening system to prevent stress corrosion cracking of reactor core shroud proceedings of the 8th international conference on nuclear engineering (ICONE-8) (Baltimore, USA); 2000.
[8] Azer M, Scheidt D. On the applications of lasers and electro optics proceedings of Icaleo'2004 (San Francisco, USA); 2004.
[9] Ballard P. Contraintes résiduelles induites par impact rapide Application au choc laser PhD thesis Ecole Polytechnique (France); 1991.
[10] Braisted W, Brockman R. Finite element simulation of laser shock peening. Int J Fatigue 1999;21:719–24.
[11] Ding K, Ye L. Three-dimensional dynamic finite element analysis of multiple laser shock peening processes. Surf Eng 2003;19:351–8.
[12] Peyre P, Sollier A, Berthe L, Bartnicki E, Fabbro R, Chaieb I, et al. FEM simulation of residual stresses induced by laser Peening. EPJ Appl Phys 2003;23:83–8.
[13] Zhang W, Yao YL, Noyan IC. Microscale laser shock peening of thin films, Part 1: experiment, modeling and simulation. J Manuf Sci Eng Trans ASME 2004;126:10–7.
[14] Ocana JL, Morales M, Molpeceres C. Experimental assessment of the influence of irradiation parameters on surface deformation and residual stresses in laser shock processed metallic alloys. Appl Surf Sci 2004;238:501–5.
[15] Hu Y, Yao Z, Hu J. 3D FEM simulation of laser shock processing. Surf Coat Technol 2006;201:1426–35.
[16] Hirano K, Sugihashi A, Imai H, Hamada N. Mecanism of anisotropic stress generation in laser peening processs. In: Proceedings of Icaleo'2006 conference (Miami, USA); 2006.
[17] Peyre P, Rouleau B, Song H, Vignal V, Amar H, Baudin T. Characterization of the mechano-electrochemical behavior of a laser – shock peened 2050–T8 aluminum alloy at global and local scales 2nd International conference on Laser Peening; 2010.
[18] Berthe L, Fabbro R, Peyre P, Tollier L, Bartnicki E. Shock waves from a water-confined laser-generated plasma. J Appl Phys 1997;82:3550–8.
[19] Peyre P, Berthe L, Scherpereel X, Fabbro R. Laser shock processing of aluminium coated 55C1 steel in water confinement regime, characterization and application to high cycle fatigue behaviour. J Mater Sci 1998;33:1421–9.
[20] Peyre P, Fabroo R, Merrien HB. Laser shock processing of aluminium alloys application to cycle fatigue behaviour. Mater Sci Eng 1996;A210:102–13.
[21] Vukelic S, Wang Y, Kysar JW, Yao YL. Comparative study of symmetric and asymmetric deformation on Al single crystal using micro-scale shock-peening. J Mech Mater Struct 2008;4:89–105.
[22] Ocaña JL, Morales M, Porro JA, Molpeceres C, Blasco M, Guarneros O, Gonzalo L, Gómez-Rosas G, Rubio-González C. Residual stress fields and associated modification of surface properties in Al and Ti alloys induced by Q-switched, ns pulse, laser shock processing 1st international conference on laser peening (Houston, USA); 2008.
[23] Amar H, Vignal V, Kraweic H, Heintz O, Josse C, Peyre P. Influence of a laser – shock processing (LSP) treatment on the microelectrochemical behavior of AA2050-T8. Corros Sci 2011;53:3215–21.
[24] Song HB. Analyse expérimentale et numérique de la distribution des contraintes résiduelles induites par choc-laser dans des alliages d'aluminium PHD thesis in PIMM Arts et Métiers Paris-Tech Paris, France; 2010.